IET Microwaves, Antennas & Propagation

Research Article

IET Journals
The Institution of Engineering and Technology

Angle-based Y-shaped chipless radio frequency identification tag

ISSN 1751-8725
Received on 18th March 2015
Revised on 27th July 2015
Accepted on 31st July 2015
doi: 10.1049/iet-map.2015.0197
www.ietdl.org

Caixia Feng, Xinwei Chen, Liping Han, Li Li, Guorui Han, Wenmei Zhang ✉

College of Physics and Electronics, Shanxi University, Shanxi 030006, People's Republic of China
✉ *E-mail: zhangwm@sxu.edu.cn*

Abstract: This study presents a novel angle-based chipless radio frequency identification tag. Its scatterer is designed to be Y-shaped. It encodes data using the space angles between the arms of the Y-shape and is identified by measuring the scattered field in two orthogonal polarisation directions. Even if it is rotated, the tag can be identified. In addition, the tag is excited with a circularly polarised wave. The cases excited with an elliptically polarised wave are also discussed. Finally, the proposed tag is realised and measured. The results indicate the realised tags operate in the frequency range 1.4–1.8 and 2.1–2.5 GHz for different codes. Every element can carry 8.1 bits of coding information. The identification errors are less than ±3.8°.

1 Introduction

Radio frequency identification (RFID) is an automated object identification method that uses radio frequency technology. The cost of the entire RFID system is dependent on the cost of the tag, which is dependent on the cost of its IC [1]. Therefore, the chipless RFID technology has been introduced.

The reported chipless RFID tags encoded data in different ways. The tag in [2] encoded data using amplitude shift keying technique which was based on the resistive properties of the organic ink. The tags in [3–5] encoded data using the spectral signature. In [3], a 5-bit space-filling curve tag was proposed, which comprised an array of five second-order Peano curves. In [4], the tag contained a vertically polarised UWB disc monopole receiving antenna, a multi-resonating circuit, and a horizontally polarised UWB transmitting tag antenna. A 24-bit RFID tag was designed in [5]. The tag operated in the frequency band of 3.1–10.6 GHz, and each data bit was associated with the presence or absence of a resonant peak at a predetermined frequency in the spectrum. The tags in [6, 7] encoded data using the amplitude/phase backscatter modulation. The toxic gas detection tag in [6] consisted of a conformal RFID antenna with a single-walled carbon nanotube composited in a chipless RFID node. The tag in [7] encoded data by means of loading scattering antennas with microstrip stubs. In recent years, some hybrid encoding tags were proposed in [8, 9]. The tag in [8] encoded data using phase and frequency. The chipless tag in [9] used multiple microstrip open stub resonators and it encoded data based on the amplitude and group delay.

In [10], a chipless tag based on three split ring resonators with variable gap configuration was proposed. It used the geometrical angle relative to the reference ring resonator to encode data. In our previous work, we proposed a novel linear chipless RFID tag that encoded data based on space angle information [11]. It was identified by the complex scattered field in two orthogonal polarisation directions. After that, we proposed a V-shaped polarisation insensitive chipless RFID tag [12], and every element can carry 3 bits of coding information.

To reveal the performance of above-mentioned tags obviously, some of their items are summarised and listed in Table 1.

In this paper, an angle-based Y-shaped chipless RFID tag is designed to increase the coding capacity. Every element can carry 8.1 bits of coding information. For different code of the tag, the proposed tag uses the same two narrow spectrums of 1.4–1.8 and 2.1–2.5 GHz. This is beneficial to reduce the cost of the RFID system and improve the spectral efficiency. The tag is excited with an elliptically polarised plane wave and it is identified by measuring the scattered field in two orthogonal polarisation directions. The Y-shaped chipless tag is designed and simulated in Section 2. To validate the practicability, the proposed tags are realised and measured in a real environment in Section 3. Finally, conclusions are drawn in Section 4.

2 Design of Y-shaped chipless RFID tag

2.1 Theory of the Y-shaped chipless RFID tag

Fig. 1 shows the structure of the Y-shaped chipless tag. It consists of a Y-shaped metal scatterer on one side of a dielectric substrate. The used substrate is Rogers 4350 with a relative permittivity of 3.66, thickness of 0.8 mm, and a loss tangent of 0.002. The Y-shaped scatterer consists of three arms (arms A, B and C) having the identical widths of w and the different lengths of l_1, l_2 and l_3 ($l_1 > l_2 > l_3$), respectively. The angle between arms A and B is α, and that between arms B and C is β. These two angles are used to encode the data. The angle of arm B with respect to x-axis is θ, which is the rotated angle of the tag.

The tag is excited with an elliptically polarised plane wave propagating along the -z-axis with an axis ratio AR. It can operate at two frequencies f_1 and f_2 ($f_1 < f_2$). The lower frequency f_1 is decided by arm A and arm B and the high frequency f_2 is decided by arm B and arm C. At f_1, the backscatter electric field components in the x and y directions E_{x-f_1} and E_{y-f_1} can be expressed as

$$E_{x-f_1} = \sqrt{\mathrm{AR}^2[E_B\cos\theta - E_A\cos(\theta+\alpha)]^2 + [E_B\sin\theta - E_A\sin(\theta+\alpha)]^2} \quad (1)$$

$$E_{y-f_1} = \sqrt{\mathrm{AR}^2[E_B\sin\theta - E_A\sin(\theta+\alpha)]^2 + [E_B\cos\theta + E_A\cos(\theta+\alpha)]^2} \quad (2)$$

Similarly, at f_2, the corresponding field E_{x-f_2}, E_{y-f_2} can be expressed

Table 1 Comparison of different chipless RFID tags

Signature used to encode	Ref.	Resonator type	Bits by single resonator	Polarisation-independent
amplitude shift keying	[2]	dual-rhombic loop	2.3 bits	no
spectral signature	[3]	space-filling curve	1 bit	no
	[4]	spiral	1 bit	no
	[5]	open-ended slot	1 bit	no
amplitude/phase backscatter modulation	[7]	microstrip stubs	1 bit	no
amplitude and group delay	[9]	open stub	1 bit	no
phase and frequency	[8]	C-shaped	2 bits	no
angle	[10]	split-ring	2 bits	no
	[11]	space angle	4 bits	no
	[12]	space angle	3 bits	yes
	this paper	space angle	8.1 bits	yes

as

$$E_{x-f_2}=\sqrt{\mathrm{AR}^2[E_B\cos\theta-E_C\cos(\beta-\theta)]^2+[E_B\sin\theta-E_C\sin(\beta-\theta)]^2}-\cos\gamma\cos\gamma E_{A-f_2} \tag{3}$$

$$E_{y-f_2}=\sqrt{\mathrm{AR}^2[E_B\sin\theta-E_C\sin(\beta-\theta)]^2+[E_B\cos\theta+E_C\cos(\beta-\theta)]^2}+\cos\gamma\sin\gamma E_{A-f_2} \tag{4}$$

where E_A, E_B, and E_C are the backscatter electric field for arms A, B, and C at their each resonant frequency, respectively, and we can obtain them by measuring the calibration tags. $\gamma=\alpha+\theta$ and E_{A-f_2} is the backscatter electric field of arm A at f_2. $\cos\gamma\cos\gamma E_{A-f_2}$ and $\cos\gamma\sin\gamma E_{A-f_2}$ are orthogonal backscatter electric field components caused by arm A at f_2.

To obtain the E_A, the linear tag having the dimension $2l_1\times w$ is used as the calibration tag, as shown in Fig. 2. It is arranged along the x-axis and excited with the same plane wave as that in Fig. 1. Its backscatter electric field component in the x direction can be measured and denoted as E_1. The length of calibration tag is double of that of arm A. Therefore, E_1 is double of E_A. That is

$$E_A=\frac{1}{2}E_1 \tag{5}$$

Similarly, the linear tags with the dimensions $2l_2\times w$ and $2l_3\times w$ are used as calibration tags to obtain the E_B and E_C, respectively. Their backscatter electric field component in the x direction E_2 and E_3 are double of E_B and E_C, respectively. That is

$$E_B=\frac{1}{2}E_2 \tag{6}$$

$$E_C=\frac{1}{2}E_3 \tag{7}$$

In this case, in (1)–(2) and (3)–(4), E_A, E_B, E_C and E_{A-f_2} are obtained first. Once the E_{x-f_1}, E_{y-f_1}, E_{x-f_2} and E_{y-f_2} for a Y-shaped tag are measured, α and β in the range of 0°–180° and the corresponding θ can be obtained. Therefore, α and β can be used to encode data and can be identified by measuring the scattered field in two orthogonal polarisation directions. It is worth noting that both θ calculated from (1)–(2) and (3)–(4) are the angles of arm B with respect to x-axis. However, because of the coupling of arms, they are not exactly the same.

To validate the coding theory, Y-shaped tags are simulated using CST Microwave Studio. Here, both α and β are selected in the range of 20–180° with 10° intervals. In this case, 289 coded combinations of α and β can be obtained. Therefore, the proposed Y-shaped tag can encode about 8.1 bits. Some typical results are shown in sections *B*, *C*, and *D*. For the convenience of distinction, the identified results of α and β are denoted as α' and β', and the corresponding θ are denoted as θ' and θ'', respectively.

2.2 Simulated results in case of $\theta=0°$ and AR = 0

In this section, the case that $\theta=0°$ (The arm B is arranged along the x-axis) is discussed. The dimensions of the tags are $l_1=40$ mm, $l_2=35$ mm, $l_3=20$ mm and $w=0.5$ mm. Without the loss of generality, the reading distance r and incident electric field intensity E_i are set as 1 m and 1 V/m, respectively. Figs. 3–4 shows some typical results

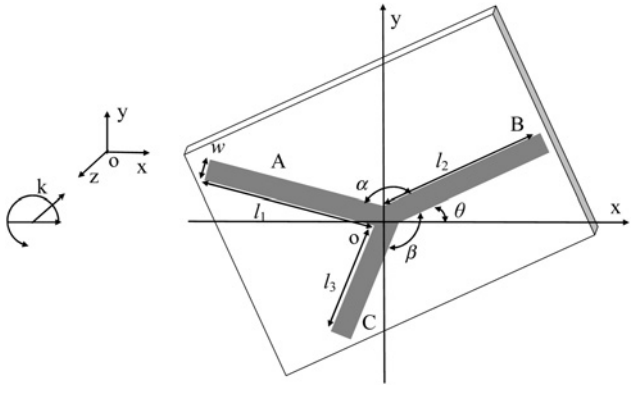

Fig. 1 *Layout of Y-shaped chipless tag*

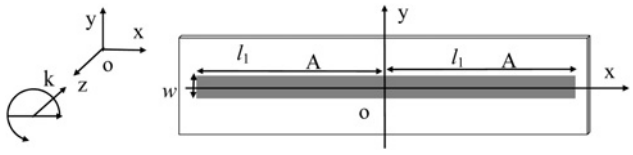

Fig. 2 *Layout of the linear calibration tag of arm A*

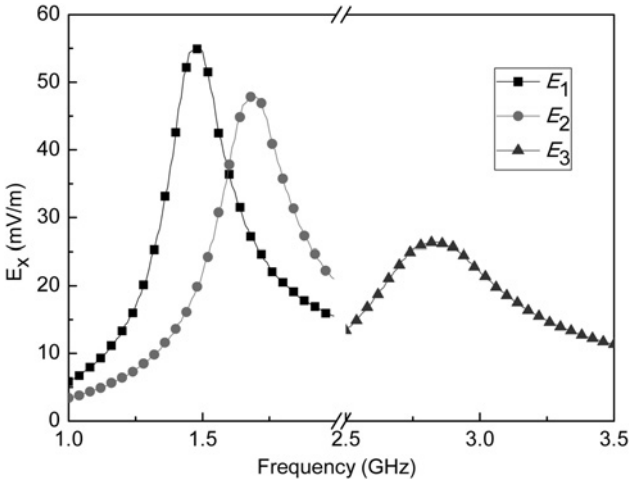

Fig. 3 *Simulated E_x for the three calibration tags in case of AR = 0 dB*

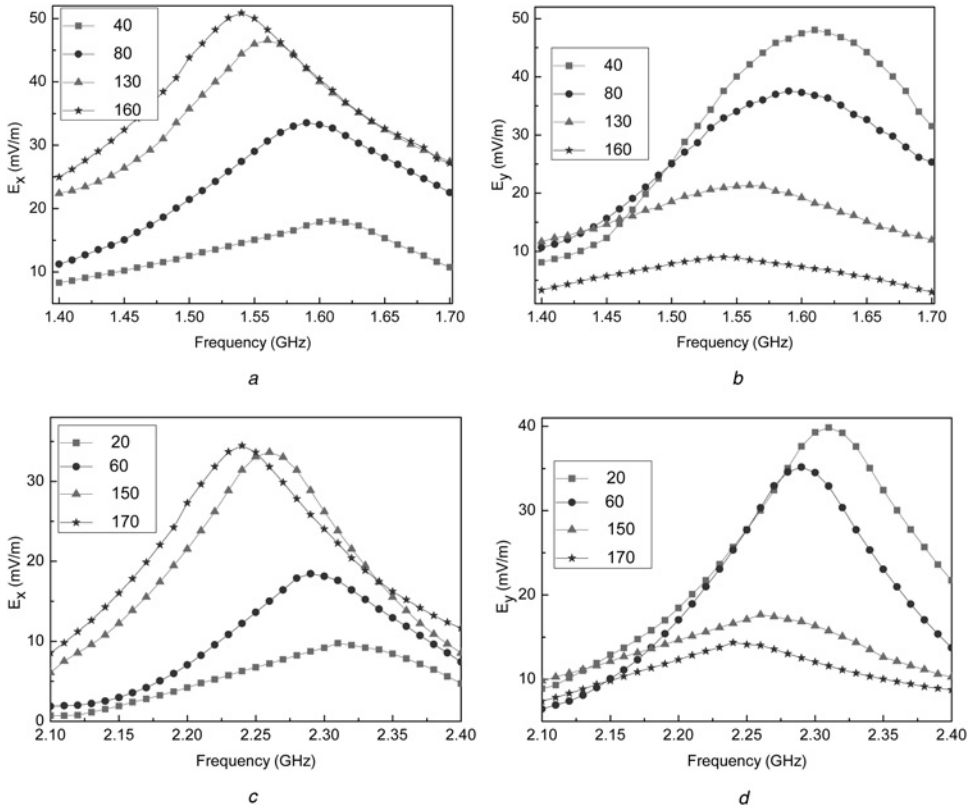

Fig. 4 *Simulated results for the Y-shaped tags in case of $\theta = 0°$ and AR = 0 dB*

a E_{x-f_1} for different α when $\beta = 150°$
b E_{y-f_1} for different α when $\beta = 150°$
c E_{x-f_2} for different β when $\alpha = 130°$
d E_{y-f_2} for different β when $\alpha = 130°$

for the tags excited with a circularly polarised incident wave. Fig. 3 shows E_x of three calibration tags. It indicates that $E_1 = 55$ mV/m, $E_2 = 48$ mV/m and $E_3 = 26.4$ mV/m at the resonant frequencies. Substituting E_1 into (5), we obtain $E_A = 27.5$ mV/m. Similarly, $E_B = 24$ mV/m and $E_C = 13.2$ mV/m. Figs. 4*a–b* show the E_{x-f_1}, E_{y-f_1} for different α when $\beta = 150°$, respectively. With the increase of α from 40° to 160°, E_{x-f_1} is gradually increased and E_{y-f_1} is gradually decreased. The same rule exists between E_{x-f_2}, E_{y-f_2} and β, as shown in Figs. 4*c–d*, respectively. Then, we will reveal how to identify the tag using the (1)–(4). Take the tag with $\alpha = 130°$, $\beta = 150°$ for example. At $f_1 = 1.56$ GHz, $E_{x-f_1} = 46.5$ mV/m and $E_{y-f_1} = 21.3$ mV/m. Substituting E_A, E_B, E_{x-f_1} and E_{y-f_1} into (1) and (2), we obtain $\alpha' = 128.9°$ and $\theta' = 1.3°$. Therefore, $\gamma = \alpha' + \theta' = 130.2°$. Meanwhile, at $f_2 = 2.26$ GHz $E_{x-f_2} = 33.3$ mV/m, $E_{y-f_2} = 17.6$ mV/m and $E_{A-f_2} = 6.4$ mV/m. Substituting E_B, E_C, E_{A-f_2}, γ, E_{x-f_2} and E_{y-f_2} into (3) and (4), we obtain $\beta' = 148.5°$ and $\theta'' = 0.3°$. It indicates that the calculated angles are approximately equal to the real ones. The simulated results for all tags in Fig. 4 are listed in Table 2. It indicates that all the errors between α and α' or β and β' are <2.1°.

2.3 Simulated results in case of $\theta \neq 0°$ and AR = 0

The rotated Y-shaped Tags are also investigated. Fig. 5 shows two typical results. Fig. 5*a* shows the backscatter field of the Y-shaped tag with $\alpha = 130°$, $\beta = 150°$, and $\theta = 10°$. At 1.55 GHz, $E_{x-f_1} = 46.9$ mV/m and $E_{y-f_1} = 14.1$ mV/m. Substituting E_A, E_B, E_{x-f_1}, and E_{y-f_1} into (1) and (2), we obtain $\alpha' = 131.1°$ and $\theta' = 9°$. Therefore, $\gamma = \alpha' + \theta' = 140.1°$. Meanwhile, $E_{x-f_2} = 32.4$ mV/m, $E_{y-f_2} = 14.1$ mV/m and $E_{A-f_2} = 6.3$ mV/m at $f_2 = 2.28$ GHz. Substituting E_B, E_C, E_{A-f_2}, γ, E_{x-f_2} and E_{y-f_2} into (3) and (4), we obtain $\beta' = 150.8°$ and $\theta'' = 11.2°$. Fig. 5*b* shows results for the Y-shaped tag with $\alpha = 160°$, $\beta = 110°$, and $\theta = -10°$. Using the

Table 2 Simulated results for some Y-shaped tags

Angles		Identified results at f_1				Identified results at f_2			
α (°)	β (°)	E_{x-f_1} (mV/m)	E_{y-f_1} (mV/m)	α' (°)	Error (°)	E_{x-f_2} (mV/m)	E_{y-f_2} (mV/m)	β' (°)	Error (°)
40	150	18	48	40.1	0.1	38.1	11.9	149.5	−0.5
80		33.5	37.5	80.8	0.8	36.1	13	151.3	1.3
130		46.5	21.3	128.9	−1.1	33.6	17.6	148.5	−1.5
160		50.8	9	161	1	33.2	17.7	151.5	1.5
130	20	46.4	21.4	128.4	−1.6	9.7	39.8	19	−1
	60	46.3	21.5	127.9	−2.1	18.4	35.1	60.7	0.7
	150	46.5	21.3	128.9	−1.1	33.6	17.6	148.5	−1.5
	170	46.5	21.2	128.8	−1.2	34.4	14.3	168.6	−1.4

IET Microw. Antennas Propag., 2015, Vol. 9, Iss. 15, pp. 1778–1785

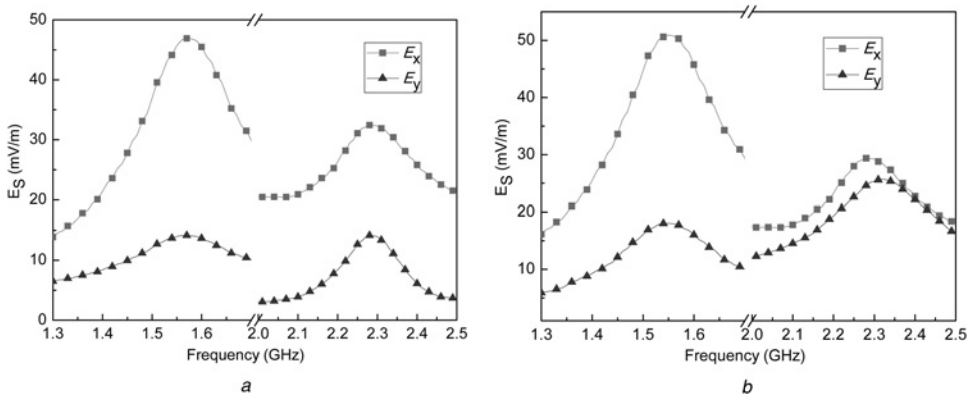

Fig. 5 *Simulated results in case of $\theta \neq 0°$ and AR = 0 dB*

a $\alpha = 130°$, $\beta = 150°$, and $\theta = 10°$
b $\alpha = 160°$, $\beta = 110°$, and $\theta = -10°$

Table 3 Simulated results for some rotated Y-shaped tags

Angles			Identified results at f_1				Identified results at f_2			
α (°)	β (°)	θ (°)	E_{x-f_1} (mV/m)	E_{y-f_1} (mV/m)	α' (°)	Error (°)	E_{x-f_2} (mV/m)	E_{y-f_2} (mV/m)	β' (°)	Error (°)
100	140	−10	40	38.3	101.6	1.6	36.9	22	142.6	2.6
130	150	10	46.9	14.1	131.1	1.1	32.4	14.1	150.8	0.8
140	120	10	48.7	10	141.9	1.9	27.8	27.7	118.7	−1.3
150	110	10	50	5	152.2	2.2	25.9	19	111.8	1.8
160	110	−10	50.9	18	162.4	2.4	29.3	25.7	110.5	0.5

same method, the calculated angles are $\alpha' = 160.7°$, $\theta' = -9.7°$, $\beta' = 110.6°$, and $\theta'' = -13°$.

The simulated results for some rotated tags are summarised and listed in Table 3. All the errors between α and α' or β and β' are less than 2.6°. It indicates that even if the Y-shaped tags are rotated at different angles, they can be identified.

2.4 Simulated results in case of $\theta \neq 0°$ and AR $\neq$ 0

In this section, the rotated Y-shaped tags excited with an elliptically polarised plane wave are investigated. Fig. 6 shows the results when AR $\neq$ 0 dB. Fig. 6*a* shows results for the Y-shaped tag with $\alpha = 130°$, $\beta = 150°$, and $\theta = 10°$ when AR = 3 dB. At 1.57 GHz, $E_{x-f_1} = 64.1$ mV/m and $E_{y-f_1} = 19.2$ mV/m. Substituting E_A, E_B, E_{x-f_1} and E_{y-f_1} into (1) and (2), we obtain $\alpha' = 130.3°$ and $\theta' = 9.7°$. Therefore, $\gamma = \alpha' + \theta' = 140°$. Meanwhile, $E_{x-f_2} = 42.2$ mV/m, $E_{y-f_2} = 18.4$ mV/m and $E_{A-f_2} = 8.9$ mV/m at $f_2 = 2.28$ GHz. Substituting E_B, E_C, E_{A-f_2}, γ, E_{x-f_2} and E_{y-f_2} into (3) and (4), we obtain $\beta' = 152.6°$ and $\theta'' = 11.6°$. Fig. 6*b* shows results for the Y-shaped tag with $\alpha = 160°$, $\beta = 110°$, and $\theta = -10°$ when AR = 2 dB. Using the same method, the calculated angle are $\alpha' = 161.9°$, $\theta' = -10.6°$, $\beta' = 110.9°$, and $\theta'' = -8.2°$.

The simulated results for some rotated Y-shaped tags when AR = 2 dB and AR = 3 dB are summarised and listed in Table 4. All the errors between α and α' or β and β' are <2.6°. It indicates that even if the rotated Y-shaped tags are excited with an elliptically polarised plane wave, they can be identified.

3 Measurement results

3.1 Measurement setup

To validate the design theory, three calibration tags and four typical Y-shaped tags are realised and measured in a real environment, not

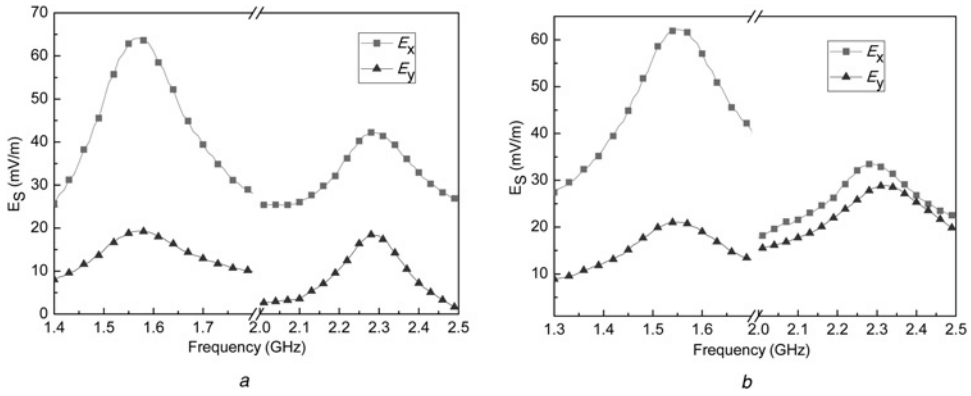

Fig. 6 *Simulated results for tags*

a $\alpha = 130°$, $\beta = 150°$, $\theta = 10°$, and AR = 3 dB
b $\alpha = 160°$, $\beta = 110°$, $\theta = -10°$, and AR = 2 dB

Table 4 Simulated results when AR = 2 dB and 3 dB

Axial ratio, dB	Angles			Identified results at f_1				Identified results at f_2			
	α (°)	β (°)	θ (°)	E_{x-f_1} (mV/m)	E_{y-f_1} (mV/m)	α' (°)	Error (°)	E_{x-f_2} (mV/m)	E_{y-f_2} (mV/m)	β' (°)	Error (°)
2	90	100	10	42	35	89.7	−0.3	31.2	32.9	100.7	0.7
	140	120	15	60.8	6.8	142.2	2.2	34.7	34.6	121.5	1.5
	150	80	−10	59.8	27	148.2	−1.8	26	30.7	78.6	−1.4
	160	110	−10	62.2	21	161.9	1.9	33.4	28.9	110.9	0.9
3	100	130	20	53.5	21	99.8	−0.2	35.3	22.8	129.5	−0.5
	110	110	20	57	20	108.5	−1.5	28.4	27.3	112.3	2.3
	120	130	30	61.8	6	118.2	−1.8	27.9	22.3	130.5	0.5
	130	150	10	64.1	19.2	130.3	0.3	42.2	18.4	152.6	2.6

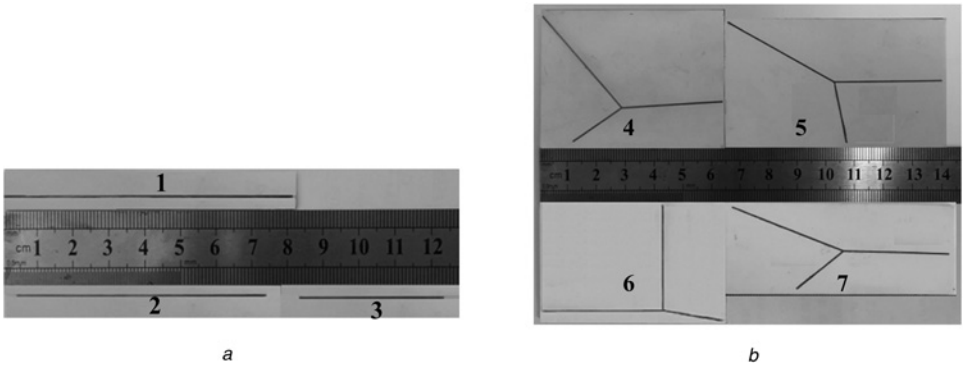

Fig. 7 *Photographs of tags*

a Calibration tags 1, 2, 3 for arm *A*, *B* and *C*
b Y-shaped tags: tag 4: $\alpha = 130°$, $\beta = 150°$. tag 5: $\alpha = 150°$, $\beta = 80°$. tag 6: $\alpha = 90°$. $\beta = 100°$. tag 7: $\alpha = 160°$, $\beta = 140°$

in an anechoic chamber. Fig. 7 shows the photographs of them. Fig. 8 shows the bistatic measurement setup. Here, the vector network analyser VNA-N5230A connected with a circularly polarised transmitting antenna and a linearly polarised receiving antenna is used as the reader. The power emitted by the VNA is −10 dBm. The tag is placed $r = 1$ m away from the antennas. The gain of transmitting antenna is in the range of 6.23–8.42 dBi in the frequency band from 1.14–3 GHz. The receiving antenna is a horn antenna with the gain in the range of 10.44–17.3 dBi. To measure the scattered field in two orthogonal polarisation directions, the horn antenna is placed horizontally (the broadside along the *x*-axis), and the S_{21-x} is obtained. Then, the horn antenna is rotated 90° (the broadside along the *y*-axis), and S_{21-y} is obtained. In the real reader, we can use the dual-polarised antenna with the horizontal and vertical polarisation to get the orthogonal scattered fields.

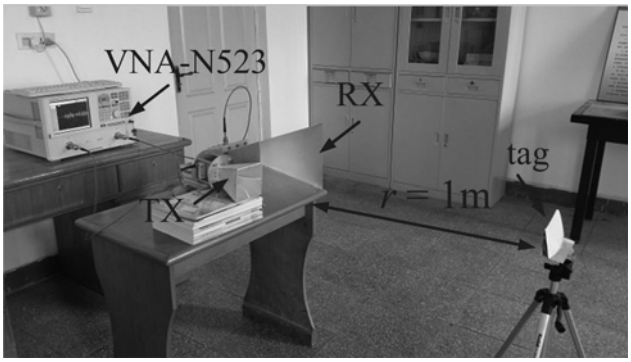

Fig. 8 *Practical measurement system setup*

3.2 Measurement theory

According to the radar equation [13], the backscattered field E_s can be expressed in term of S_{21} as

$$E_s = \frac{4\pi r}{\sqrt{G_1 G_2 \lambda}} |S_{21}| \tag{8}$$

Obviously, once the S_{21} is measured, backscattered field E_s can be obtained from (8). Substituting E_s in (1) and (2) or (3) and (4), the α or β can be calculated. Or, we can calculate α and β by substituting the corresponding $|S_{21}|$ into (1)–(4) directly [12].

3.3 Measurement procedure

The measurement is performed according to the following steps:

(i) Measure the background noise without tag S_{21-x0} and S_{21-y0}.
(ii) Measure the calibration tags and obtain S_{21-xn1}, S_{21-xn2} and S_{21-xn3}.
(iii) Measure the detected Y-shaped tag and get S_{21-xn} and S_{21-yn}.

(iv) Remove all background noise and get the actual S_{21}. For the linear calibration tags, the actual S_{21-x} are

$$S_{21-1} = S_{21-xn1} - S_{21-x0} \tag{9}$$

$$S_{21-2} = S_{21-xn2} - S_{21-x0} \tag{10}$$

$$S_{21-3} = S_{21-xn3} - S_{21-x0} \tag{11}$$

The actual S_{21} of Y-shaped detected tags can be expressed as

$$S_{21-x} = S_{21-xn} - S_{21-x0} \tag{12}$$

$$S_{21-y} = S_{21-yn} - S_{21-y0} \tag{13}$$

(v) Transform the $|S_{21-1}|$, $|S_{21-2}|$, $|S_{21-3}|$, $|S_{21-x}|$ and $|S_{21-y}|$ into the corresponding scattered electric field, then calculate the space angles α and β according to (1)–(4). Or, substitute the $|S_{21-1}|$, $|S_{21-2}|$, $|S_{21-3}|$, $|S_{21-x}|$ and $|S_{21-y}|$ into (1)–(4) directly and calculate the α and β.

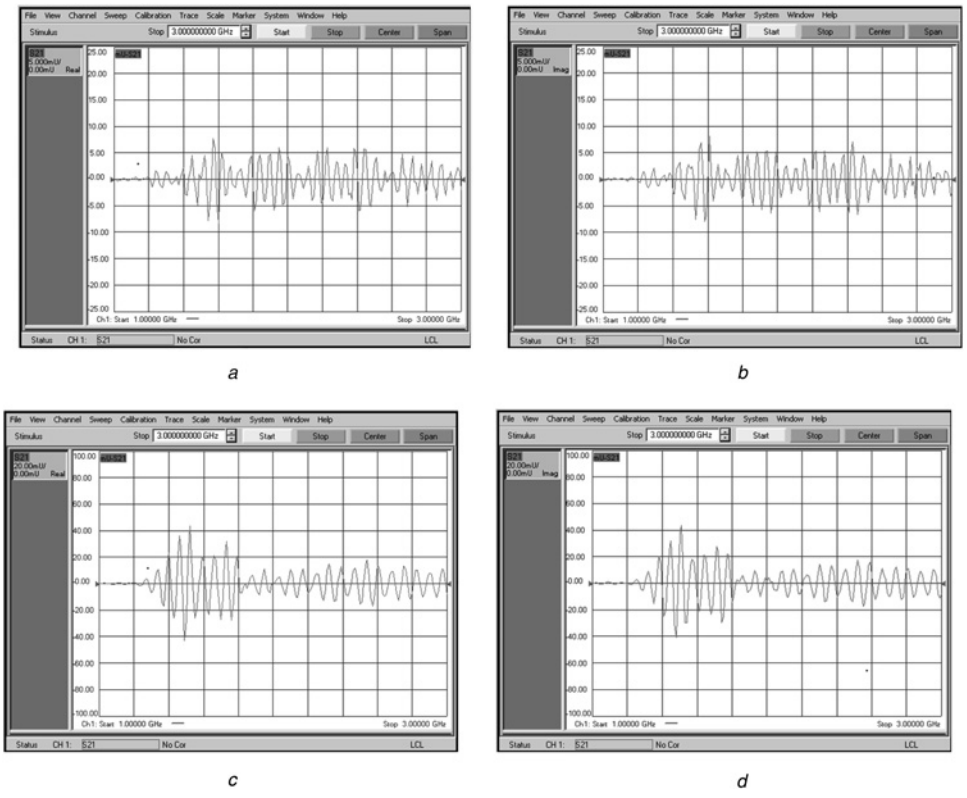

Fig. 9 *Measured S_{21-x0} and S_{21-y0} for the background noise*

a Real part of S_{21-x0}
b Imaginary part of S_{21-x0}
c Real part of S_{21-y0}
d Imaginary part of S_{21-y0}

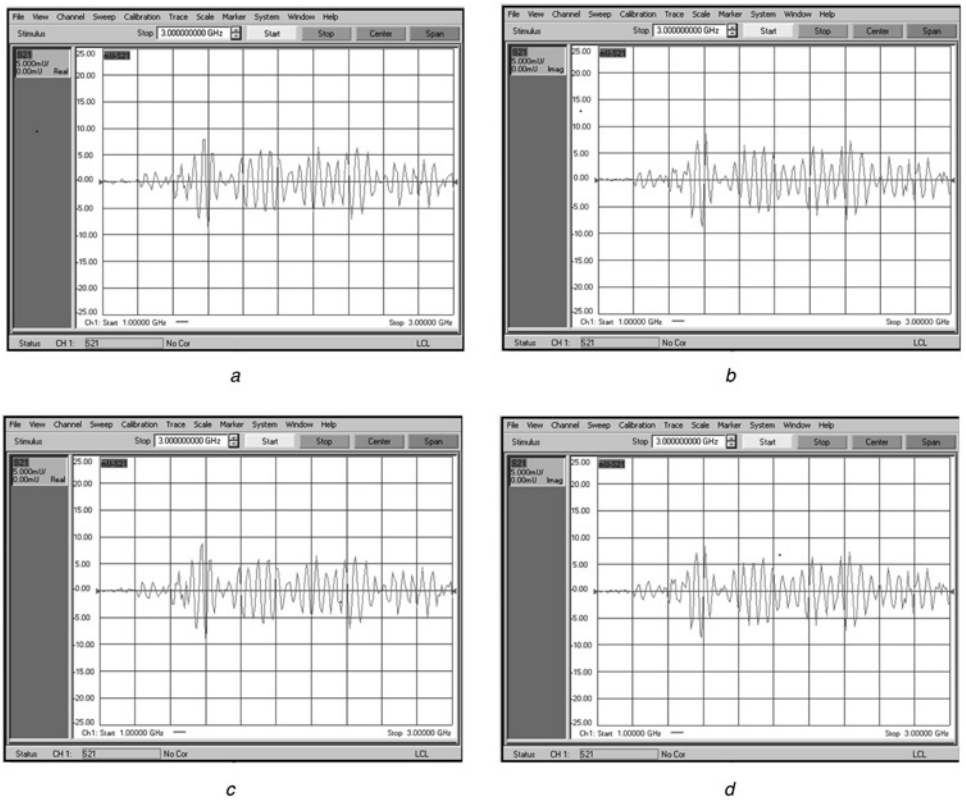

Fig. 10 *Measured S_{21-xn1} and S_{21-xn2} for the calibration tag 1 and 2*

a Real part of S_{21-xn1} for calibration tag 1
b Imaginary part of S_{21-xn1} for calibration tag 1
c Real part of S_{21-xn2} for calibration tag 2
d Imaginary part of S_{21-xn2} for calibration tag 2

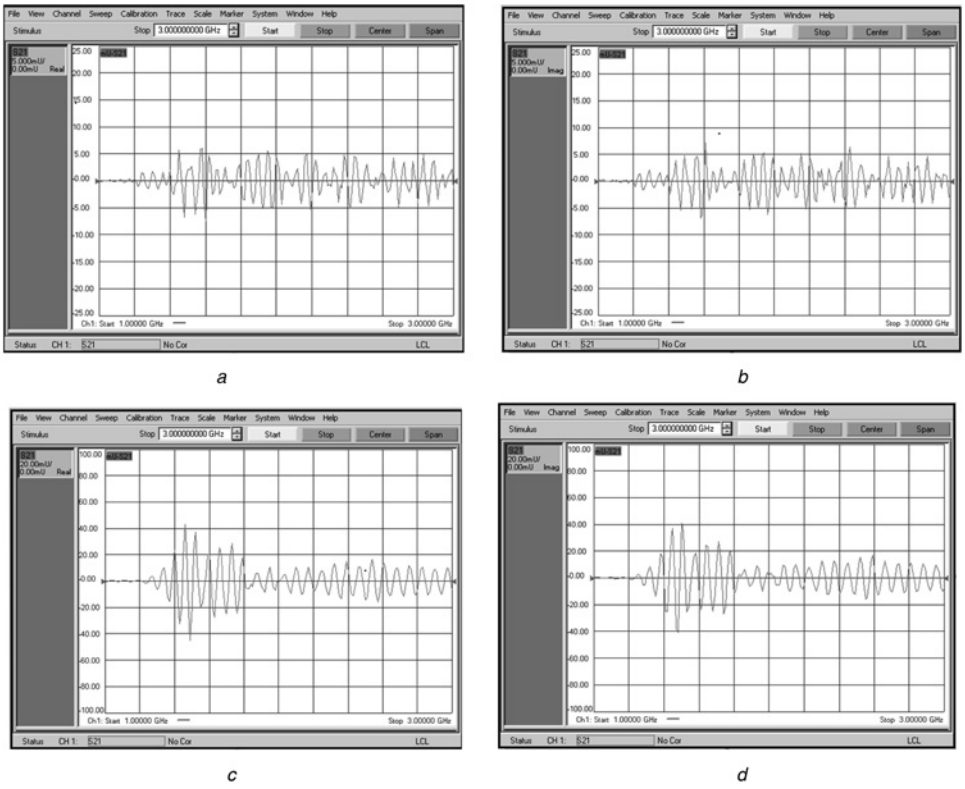

Fig. 11 *Measured S_{21-xn} and S_{21-yn} of tag 4: $\alpha = 130°$, $\beta = 150°$, $\theta = 10°$*

a Real part of S_{21-xn}
b Imaginary part of S_{21-xn}
c Real part of S_{21-yn}
d Imaginary part of S_{21-yn}

3.4 Measurement results

Figs. 9–11 shows the photo of the original measured results in measurement procedure (i)–(iii), respectively. Fig. 9 shows the measured real and imaginary parts of S_{21} for the background noise. Fig. 10 shows that for calibration tags. For simplification, only the results for the tags 1 and 2 are provided. It can be observed that curves in Figs. 10*a–b* and Figs. 10*c–d* are different from that in Figs. 9*a–b* around 1.5 GHz and 1.7 GHz, respectively. Fig. 11 shows the measured results for the identified tags. For simplification, only the results for tag 4 are provided. At about 1.6 and 2.2 GHz, the curves in Figs. 11*a–d* are different from that in Figs. 9*a–d*, respectively. It is worth noting that all of the above frequencies are the resonant frequencies of the corresponding tags. Substituting the measured real parts of S_{21-xn1} in Fig. 10*a* and S_{21-x0} in Fig. 9*a* into (9), we obtain the real part of actual S_{21-1} for the calibration tag 1. Using the same method, we can obtain the imaginary part of S_{21-1}. Then $|S_{21-1}|$ can be obtained. Similarly, $|S_{21-2}|$, $|S_{21-3}|$ for calibration tags 2–3 can be obtained. Correspondingly, according to (10)–(13), the $|S_{21-x}|$ and $|S_{21-y}|$ for the identified tag 4 can be obtained.

Fig. 12 shows all the calculated $|S_{21}|$ from the Figs. 9–11. For comparison, the simulated backscatter field E_1, E_2, E_3, E_x and E_y are transformed into $|S_{21-1s}|$, $|S_{21-2s}|$, $|S_{21-3s}|$, $|S_{21-xs}|$ and $|S_{21-ys}|$ according to (8) and shown in the corresponding figures. It is noted that the simulated and measured $|S_{21}|$ agree basically. Compared with the simulated results, the measured results shift up about 0.04 GHz. Fig. 12*a* shows the results for the calibration tags after background noises are removed. $|S_{21-1}| = 0.0102$, $|S_{21-2}| = 0.0088$ and $|S_{21-3}| = 0.005$ at their respective resonant frequencies.

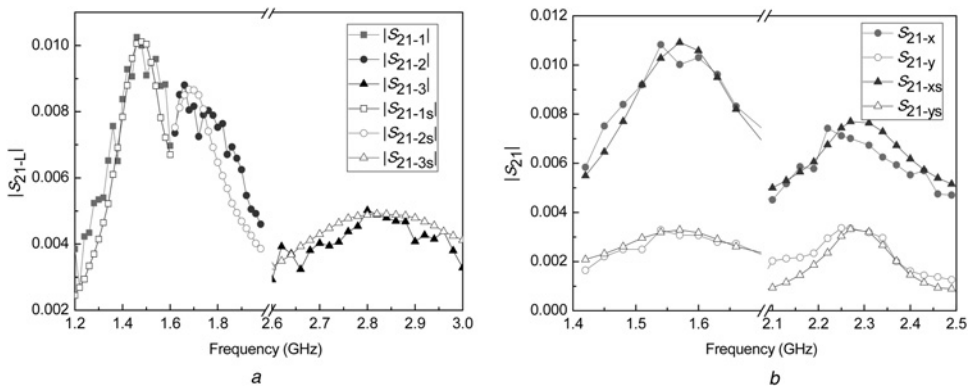

Fig. 12 *Calculated $|S_{21}|$ according to Figs. 9–11*

a $|S_{21-1}|$, $|S_{21-2}|$, $|S_{21-3}|$ for three calibration tags
b $|S_{21-x}|$ and $|S_{21-y}|$ for tag 4

Table 5 Measured results for some Y-shaped tags

Angles			Identified results at f_1				Identified results at f_2			
α (°)	β (°)	θ (°)	$\lvert S_{21-x}\rvert$	$\lvert S_{21-y}\rvert$	α' (°)	Error (°)	$\lvert S_{21-x}\rvert$	$\lvert S_{21-y}\rvert$	β' (°)	Error (°)
130	150	10	0.0105	0.0052	128.6	−1.4	0.0074	0.0033	151.6	1.6
150	80	0	0.0115	0.0035	149.2	−0.8	0.0045	0.0064	80.9	0.9
90	100	0	0.0076	0.0075	88.8	−1.2	0.0066	0.0067	96.2	−3.8
160	140	0	0.0118	0.0025	156.2	−3.8	0.0071	0.004	136.2	−3.8

Then we obtain $|S_{21-A}| = 0.0051$, $|S_{21-B}| = 0.0044$ and $|S_{21-C}| = 0.0025$ for the three arms. Fig. 12*b* shows the results for the tags 4. At 1.57 GHz, $|S_{21-x}| = 0.0109$ and $|S_{21-y}| = 0.0032$. Substituting S_{21-x}, S_{21-y}, S_{21-A} and S_{21-B} into (1) and (2), we obtain $\alpha' = 131.2°$ and $\theta' = 9.6°$. Therefore, $\gamma = \alpha' + \theta' = 140.8°$. Then we obtained $|S_{21-A-f_2}| = 0.0014$, $|S_{21-x}| = 0.0074$ and $|S_{21-y}| = 0.0033$ at $f_2 = 2.25$ GHz (AR = 2.1 dB). Substituting $|S_{21-x}|$, $|S_{21-y}|$, $|S_{21-B}|$, $|S_{21-C}|$, $|S_{21-A-f_2}|$ and γ into (3) and (4), we obtain $\beta' = 151.6°$ and $\theta'' = 6.7°$.

Finally, the measured results for the four realised Y-shaped tags are listed in Table 5. It can be seen that these tags can be identified and the identification errors are less than ±3.8°.

4 Conclusions

In this paper, a novel angle-based Y-shaped chipless tag has been introduced. It is identified by measuring the complex scattered field in two orthogonal polarisation directions. The simulated and measured results show the identification errors are less than ±3.8°. Every element of the proposed tag can carry 8.1 bits of coding information in a credit card size 76 mm × 54 mm × 0.76 mm. Moreover, for different code of the tag, the proposed tag uses the same two narrow spectrums of 1.4–1.8 and 2.1–2.5 GHz. This is beneficial to reduce the cost of the RFID system and improve the spectral efficiency.

To improve the coding capacity of per unit area, we can use higher coding frequency bands. With the increase of operating frequency, the size of the tag can be decreased and the density of coding per surface can be increased. Another way is increasing the number of arms. If we increase one arm, the density of coding can increase 4 bits. For a tag with four arms, it can encode 12 bits. As for the *-shaped tag with eight arms, it can encode 28 bits.

5 Acknowledgments

This work was supported by the National Science Foundation of China (grant no. 61271160), Shanxi Scholarship Council of China (grant no. 2012-014), the Research Fund for the Doctoral Program of Higher Education (grant no. 20121401110009), and the Natural Science Foundation of Shanxi province (grant no. 2012011013-3).

6 References

1 Stevan, P., Nemai, C.K.: 'Chipless RFID: bar code of the future', *IEEE Microw. Mag.*, 2010, **11**, (7), pp. 87–97
2 Vena, A., Babar, A.A., Sydänheimo, L., *et al.*: 'A novel near-transparent ASK-reconfigurable inkjet-printed chipless RFID tag', *IEEE Antennas Wirel. Propag. Lett.*, 2013, **12**, (6), pp. 753–756
3 McVay, J., Hoorfar, A., Engheta, N., *et al.*: 'Space-filling curve RFID tags'. IEEE Radio and Wireless Symp., January 2006, pp. 199–202
4 Preradovic, S., Karmakar, N.C.: 'Multiresonator-based chipless RFID system for low-cost item tracking', *IEEE Trans. Microw. Theory Tech.*, 2009, **57**, (5), pp. 1411–1419
5 Reza, R., Majid, M.: 'Complex-natural-resonance-based design of chipless RFID tag for high-density data', *IEEE Trans. Antennas Propag.*, 2014, **62**, (2), pp. 898–904
6 Yang, L., Zhang, R., Staiculescu, D., *et al.*: 'A novel conformal RFID-enabled module utilizing inkjet-printedantennas and carbon nanotubes for gas-detection applications', *IEEE Antennas Wirel. Propag. Lett.*, 2009, **8**, (5), pp. 653–656
7 Balbin, I., Karmakar, N.C.: 'Phase-encoded chipless RFID transponder for large-scale low-cost applications', *IEEE Microw. Wirel. Compon. Lett.*, 2009, **19**, (8), pp. 509–511
8 Vena, A., Perret, E., Tedjini, S.: 'Chipless RFID tag using hybrid coding technique', *IEEE Trans. Microw. Theory Tech.*, 2011, **59**, (12), pp. 3356–3364
9 Nijas, C.M., Dinesh, R., Deepak, U., *et al.*: 'Chipless RFID tag using multiple microstrip open stub resonators', *IEEE Trans. Antennas Propag.*, 2012, **60**, (9), pp. 4429–4432
10 Vena, A., Perret, E., Tedjini, S.: 'A compact chipless RFID tag using polarization diversity for encoding and sensing'. IEEE Int. Conf. on RFID 2012, Orlando, USA, April 2012, pp. 191–197
11 Yan, L.Y., Zhang, W.M., Ma, R.B., *et al.*: 'Chipless RFID tag based on space angle information'. IEEE MTT-S Int. Microwave Workshop Series on RF and Wireless Technologies for Biomedical and Healthcare Applications (IMWS-BIO), Singapore, 2013, pp. 1–3
12 Feng, C., Zhang, W., Li, L., *et al.*: 'Angle-based chipless RFID tag with high capacity and insensitivity to polarization', *IEEE Trans. Antennas Propag.*, 2015, **63**, (4), pp. 1789–1796
13 Richards, M.A., Scheer, J.A., Holm, W.A.: 'Principles of modern radar' (Raleigh, 2010, NC 27615: SciTech.), pp. 64–220